Effects of low pressure plasma treatments on DSSCs based on rutile TiO₂ array photoanodes

Weiqi Wang[a], Jiazang Chen[b], Jianqiang Luo[a], Yuzhi Zhang[c], Lian Gao[a],
Yangqiao Liu[a,*], Jing Sun[a,**]

[a] The state Key Laboratory of High Performance and Superfine Microstructure, Shanghai Institute of Ceramics, Chinese Academy of Sciences, 1295 Dingxi Road, Shanghai 200050, PR China
[b] Division of Chemical and Biomolecular Engineering, School of Chemical & Biomedical Engineering, Nanyang Technological University, 62 Nanyang Drive, Singapore 637459, Singapore
[c] The Key Laboratory of Inorganic Coating Materials, Shanghai Institute of Ceramics, Chinese Academy of Sciences, 1295 Dingxi Road, Shanghai 200050, PR China

ARTICLE INFO

ABSTRACT

In this paper, three types of low pressure plasma including hydrogen (HP), oxygen (OP) and nitrogen (NP) treatments have been utilized for the first time to improve DSSCs based on rutile TiO₂ array photoanodes. Their effects on the photoanodes and the cell performance have been systematically compared by characterizing the dye loading amount, flat-band potential, donor concentration, electron lifetime and the photovoltaic parameters. Experimental results show that all the three plasma treatments increase the dye loading owing to improved hydrophilicity or enhanced surface roughness. It is found that NP and OP treatments significantly increase the TiO₂ donor concentration and decrease trapping sites. By this way, the electron transport is enhanced and the electron recombination is effectively restrained. These comprehensive effects make NP and OP treatments beneficial for the overall performance, by which 13% and 5% increases in efficiency are achieved. However, HP treatment causes obvious reduction in the donor concentration and more severe electron recombination, which decreases the efficiency by about 15%.

© 2014 Elsevier B.V. All rights reserved.

1. Introduction

Since the first report in 1991 by Graetzel and coworkers [1], dye-sensitized solar cells (DSSCs) have been regarded as the promising alternative to traditional silicon based solar cells due to their low fabrication cost, facile assembly process and high light-to-electricity conversion efficiency [2–4]. Titania is now the most commonly used DSSC photoanode material as it owns physical and chemical stability under illumination in liquid electrolytes, as well as an appropriate band structure [5–7].

In recent years, one-dimensional titania materials such as nanorods [8–10], nanowires [11], nanotubes [12,13], become the focus for constructing DSSC photoanodes since they are expected to build up direct electron transport pathways. Generally, one-dimensional anatase electrodes can result in higher light-to-electricity conversion efficiencies than rutile. However, they are routinely fabricated on Ti substrate and need to be transferred to transparent FTO substrates before use. Otherwise, only back-illuminated cells with much lower efficiency can be assembled. In contrast, one-dimensional rutile DSSC can be fabricated much easily since rutile nanorod arrays can grow directly on FTO substrates by a facile hydrothermal process [14]. Furthermore, rutile has smaller bandgap (3.02 eV) and better light reflecting properties than anatase [15–17]. These combinative benefits arouse attention to rutile array as DSSC anode materials and many related studies have been reported [18–20].

In order to improve the photovoltaic performances of rutile array DSSCs, various post-treatment techniques have been developed. For example, Lv et al. [21] proposed a chemical etching method to reinforce the adhesion of rutile arrays onto FTO substrate and an efficiency of 5.94% was achieved. Wang et al. [22] found that TiCl₄ post-treatment on rutile array photoanodes could induce the formation of anatase nanoparticles, which could increase their surface area and dye loading abilities. Ling et al. [23] used hydrogenation post-treatments to increase the electron density in the rutile arrays and increased the efficiency from 0.28% to 0.45%.

* Corresponding author. Tel.: +86 21 5241 2720; fax: +86 21 52413122.
** Corresponding author. Tel.: +86 21 5241 4301; fax: +86 21 52413122.
E-mail addresses: yqliu@mail.sic.ac.cn (Y. Liu), jingsun@mail.sic.ac.cn (J. Sun).

Recently, plasma surface treatments have been applied to enhance the performance of DSSCs. For instance, Kim et al. [24] applied H_2 plasma to treat anatase nanoparticles and improved electron lifetime in the cell. Wang et al. [25] tried O_2 plasma to treat anatase nanotube arrays and achieved an optimized cell efficiency of 7.37% in a back-illuminated cell. However, most of the studies have only tried one specific type of plasmas and there is still a lack of systematic comparison about photovoltaic performance after different types of plasma treatments, especially in one-dimensional rutile array electrodes.

In this paper, three types of low pressure plasma including hydrogen (marked as HP), oxygen (OP), and nitrogen (NP) have been used to treat rutile array photoanodes of DSSCs. By taking tests on Mott–Schottky (MS) plot, impedance electrochemical spectroscopy (EIS) and open-circuit voltage decay (OCVD), the effects of different plasma treatments on the electrode's flat-band potential, the electron transport and the electron recombination behavior are systematically investigated. Based on the above results, the effect of plasma treatments on the light-to-electricity conversion efficiency of DSSCs is finally discussed. It is expected that this paper can give an overall understanding of the plasma treatment effect on the electrochemical properties of TiO_2 and provide basis for the selection of appropriate plasma treatments for improving DSSCs.

2. Experiment

2.1. Fabrication of rutile array photoanode

The fabrication of the rutile array photoanode was modified from a literature procedure [21]. In brief, FTO substrates were ultrasonically rinsed in ethanol, deionized (DI) water, acetone and ethanol sequentially and further dried at 60 °C. 0.5 ml of titanium tetrabutoxide $(Ti(OBu)_4)$ was added into 20 ml 1:1 hydrochloric acid, followed by 10 min of ultrasonication to obtain a transparent solution. Then four pieces of as-cleaned FTO substrate were set into a 40 ml Teflon autoclave vertically with a customized holder. A hydrothermal treatment process was carried out at 170 °C for 6 h, and thereafter the autoclave was cooled down to room temperature. After the samples were rinsed with DI water, it was further chemically etched by another hydrothermal process using hydrochloric acid (1:1, vol:vol) at 150 °C for 4 h. After rinsed with DI water for several times, the samples were calcined at 450 °C for 30 min.

2.2. Plasma surface treatment

As-fabricated photoanodes were subjected to a low pressure plasma treatment. Under 140 W RF power, one of the three process gas (hydrogen, oxygen, nitrogen) was introduced at a constant working pressure. All plasma treatments were taken for 10 min (See photographs in SI).

2.3. Assembly of DSSCs

The photoanodes were immersed for 24 h in 0.3 mM N719 (Di-tetrabutylammonium *cis*-bis(isothiocyanato)bis(2,2′-bipyridyl-4,4′-dicarboxylato)-ruthenium(II)) dye solution in acetonitrile/tert-butanol (1:1, vol:vol) mixed solvent. The electrode was then rinsed with acetonitrile and dried. Then one drop of electrolyte, composed of 0.1 M lithium iodide (LiI), 0.6 M tetrabutylammonium iodide (TBAI), 0.05 M iodine (I_2), and 0.5 M 4-tert-butylpyridine dissolved in acetonitrile, was deposited onto the electrode. A sputtered platinum FTO counter electrode was clipped on to form a photovoltaic cell for further characterization.
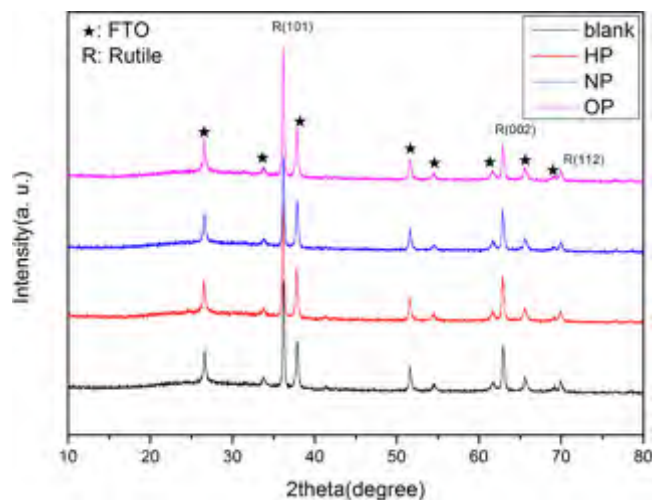

Fig. 1. XRD patterns of plasma treated rutile nanorod arrays.

2.4. Characterizations of samples

Compositions of the samples were investigated by X-ray diffraction (XRD, D/max 2550 V, Rigaku Tokyo) and Raman spectroscopy (DXR Raman Microscope with an excitation length of 532 nm, Thermo Fisher). The morphology was characterized with field emission electron microscope (FESEM, Hitachi S4800). Water contact angle (WCA) was measured by automatic contact angle meter (Model SL200B, China) to characterize the surface hydrophilicity. X-ray photoelectron spectroscopy (XPS) analysis was conducted using Al Kα (ESCAlab250, Thermo Fisher Scientific). Electrochemical impedance spectroscopy (EIS) measurements were carried out on a CHI 660D electrochemical workstation and further fitted by Z-view software. The Mott–Schottky (MS) plot measurement was performed by a potentiodynamic impedance spectroscopy applying a tri-electrode system on CHI 660D. The dark currents were characterized by taking linear sweep voltammetry (LSV) measurements with an applied bias set from 0 to 1.1 V. The electron lifetime determined by open-circuit voltage decay (OCVD) measurements was recorded on Solartron 1400A analytical center with a potentiostat. The photocurrent–voltage (I–V) curves were recorded using Keithley 2400 meter under simulated AM1.5G solar irradiation (100 mW/cm²).
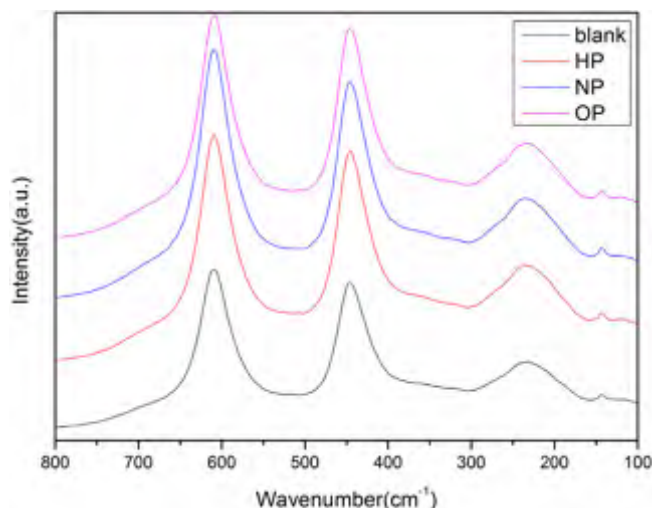

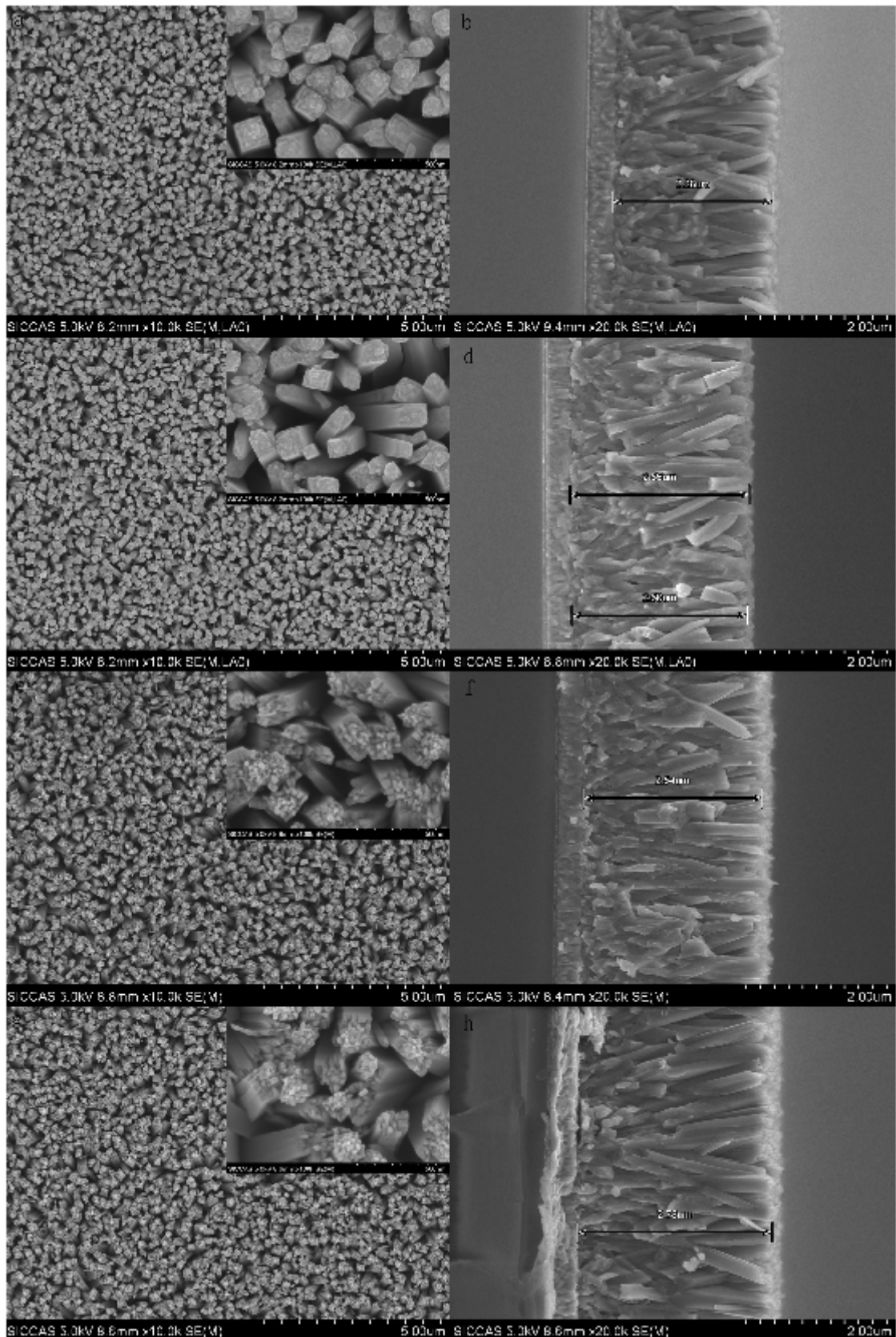**Fig. 2.** Raman spectra of plasma treated rutile nanorod arrays.

Fig. 3. FESEM images of the top and cross-sectional views of plasma treated rutile arrays. The images are blank samples without plasma treatment (a and b), HP (c and d), OP (e and f), NP (g and h), respectively. Inset images are the top views of the magnified details in the selected area.

3. Results and discussion

3.1. Morphologies

Fig. 1 shows the XRD patterns of the rutile arrays grown on the FTO substrate and those after hydrogen, nitrogen or oxygen plasma treatments. From the patterns we can figure out the highest diffraction peak of $(1\,0\,1)$, followed by a weaker $(0\,0\,2)$, indicating that the rutile crystals grow with $(1\,0\,1)$ plane parallel to the substrate and the nanorods with the direction of $(0\,0\,2)$ [26]. Fig. 2 shows the Raman spectra of the prepared samples. Three sharp peaks located at 144.10, 445.91 and 610.79 cm^{-1} all refer to B_{1g}, E_g, A_{1g} mode of rutile, respectively and the broad band near 231 cm^{-1} is a second-order phonon of rutile [27,28]. These signify the formation of rutile TiO$_2$. From Fig. 1 and 2, no obvious changes in the XRD patterns and Raman spectra can be noticed after three types of plasma post-treatment, suggesting that these treatments do not alter the rutile crystalline phase of TiO$_2$.

Fig. 3 shows the FESEM images of the grown rutile array. It can be seen that densely aligned TiO$_2$ nanorod arrays with a diameter of ca. 150 nm are uniformly grown on the FTO substrate. From the cross-sectional view of the film, it can be found that the lengths of the nanorod arrays are ca. 2.5 μm.

Furthermore, comparing the top view of the images, we can find out that the tops of the four samples, blank, OP, HP, and NP possess clearly different morphologies. The blank and HP samples are relatively smooth with no sharp edges. However, for the OP and NP samples, each nanorod tip possesses over ten of protruding sharp pillars, i.e., the nanorod tips become much rougher. These sharper characteristics of OP and NP samples can also be seen from the cross-sectional view shown as Fig. 3f and h. These structural changes should result from the etching of the unstable chemical states at the rutile grain boundary by plasmas [29]. The much significant morphological changes of OP and NP samples can be attributed to the higher physical etching abilities of oxygen and nitrogen plasmas as reported in previous researches [30]. The negligible morphological change after HP treatment means that hydrogen plasma treatment has milder etching abilities, which is consistent with the report that hydrogen plasma is much weaker than oxygen plasma [31,32]. As a result, the HP suffers little from the plasma treatment while the other two present obvious footsteps caused by the stronger etching effects. However, no differences can be discerned in XRD patterns and Raman spectra, indicating that these physical etching does not harm the main structure of the rutile nanorod arrays.

3.2. Light absorption and dye adsorption

Usually, post treatments of the photoanodes may affect the cell performance through two pathways, one is enhancing light harvest efficiencies and the other is improving the carrier transfer abilities. The former is often achieved by more light absorption and higher dye loading amount [33,34]. Fig. S2 shows the UV–vis transmission spectra of FTO/TiO$_2$ electrodes. The curves of the electrodes with and without plasma treatments demonstrate nearly no difference, meaning that the numbers of photons exposed to the TiO$_2$-dye interface are almost the same. On the other hand, dye adsorption results in Table 1 indicate an obvious increase of dye loading after plasma treatment, from 31.7 nmol/cm^2 for blank to 38.8, 42.9, 41.3 nmol/cm^2 for NP, HP, OP, respectively. The increments of dye loading amounts imply that under the same illumination condition, the number of photo-induced electrons that inject into the conduction band of titania increases after plasma treatments.

In order to explore the reasons for these dye adsorption increments, we investigate the difference in hydrophilicity of the samples by measuring their water contact angles (WCAs) and

Table 1
Summary of WCA and dye-loading of plasma treated electrodes.

Samples	WCA (°)	Dye loading (nmol/cm^2)
Blank	34.4	31.7
HP	14.6	42.9
NP	34.2	38.8
OP	10.0	41.3

Table 2
Summary of calculated parameters of Mott–Schottky plots.

Samples	V_{fb} vs. Ag/AgCl (V)	N_d ($\times 10^{15}$/cm^{-3})
Blank	−0.458	8.51
HP	−0.386	5.54
NP	−0.446	12.9
OP	−0.421	9.30

the results are shown in Table 1. It can be seen that the WCAs decrease from 34.4° for blank sample to 14.6° and 10.0° for HP and OP, respectively. This clearly shows that the hydrophilicity of the rutile array electrode is remarkably enhanced after hydrogen and oxygen plasma treatments. This is within expectation as previous researches have pointed out that the material surfaces can be converted to a −OH group abundant surface after hydrogen and oxygen plasma treatment [31,35]. Such a great enhancement in hydrophilicity leads to a 30.3% and 35.3% increase of the dye adsorption for HP and OP, respectively. In contrast, only a minor change of the hydrophilicity takes place after nitrogen plasma treatment, as the WCA of NP (34.2°) is almost identical to that of blank sample (34.4°). Therefore, the 22.4% increment in dye adsorption of NP should mainly be attributed to the increased roughness of the NP.

Briefly, all three plasma treatments could enhance the dye adsorption and generate more photo-induced electrons.

3.3. Band edge movements

Fig. 4 shows the MS plot of the photoanodes acquired by potentiodynamic electrochemical impedance spectroscopy. A standard three-electrode system was utilized for the measurements with FTO/TiO$_2$ as the working electrode, platinum wire as the counter electrode and Ag/AgCl electrodes as the reference, respectively. The electrolyte used was 0.1 M LiClO$_4$ in carbonate propylene in order to avoid double layer capacitance interference in aqueous solution.
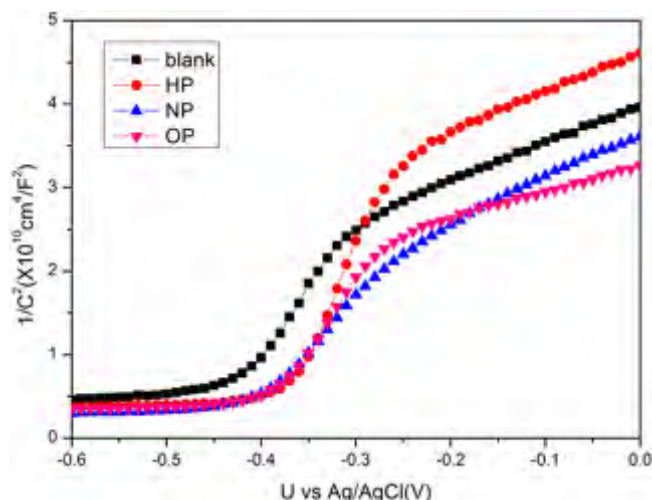

Fig. 4. Mott–Schottky plots of plasma treated rutile nanorod arrays.

The flat-band potential (V_{fb}) and donor concentration (N_d) results are listed in Table 2, which is calculated through Eq. (1):

$$\frac{1}{C^2} = \left(\frac{2(V - V_{fb} - k_B T/e_0)}{\varepsilon \varepsilon_0 e_0 N_d A^2} \right) \tag{1}$$

where ε_0 is the permittivity of free space, ε is the relative permittivity of rutile (in this case, we used $\varepsilon = 180$[36], the value along the c-axis, to evaluate the N_d), e_0 is the elementary charge, k_B is the Boltzmann constant, T is the temperature and A stands for surface area. The slope is inversely proportional to N_d and V_{fb} is determined when $1/c^2 = 0$.

As Mora-Sero et al. [37] previously uncovered, the ZnO nanorod array cannot be simply treated as flat surfaces, since each nanorod owns its depletion layer that grows toward the nanorod center. Thus, in this work, the calculation of effective surface area of rutile nanorod array should also include the side surface area increment. According to SEM images in Fig. 3, the average rod density and the average rod size are estimated to be 1.4×10^9/cm^2 and 160 nm $\times$ 160 nm $\times$ 2500 nm (each rod seen as a cuboid), respectively. Since each nanorod increases surface area by 1.6×10^{-8} cm^2, the effective surface area of nanorod array is estimated to be 23.4 cm^2 per square centimeter. Besides, the equivalent circuit measuring the capacitance of thin film can be described as an electrolyte resistance in series with a parallel association of the charge transfer resistance and the space charge capacitance [37–40]. The parallel charge transfer resistance obtained from frequency dependence of impedance measurement (see SI, Fig. S3) is estimated to be 0.56 MΩ, a high resistance that ensures the charge transfer is avoided during measurements.

From Table 2, we can see that the V_{fb} of the blank sample, HP, NP, OP are $-0.458, -0.386, -0.446$ and -0.421 V, respectively. Namely, all three plasma-treated samples demonstrate a positive shift of V_{fb}. It has been widely reported that oxides bounded to TiO$_2$ [41,42] highly influence its V_{fb} value. In this case, for HP and OP, the —OH surface groups added through plasma treatment affect the chemical environment of TiO$_2$-solution interface, leading to an more obvious positive movement of V_{fb}. Yet for NP, as the sample owns slightest hydrophilicity change, the smallest V_{fb} shift means the least surface group modified among three plasma treated samples. It is widely known that the gap between V_{fb} and E_{redox} of I^-/I_3^- couple determines the open circuit voltage (V_{oc}). Therefore, all the three types of plasma treatments are expected to cause a decrease in V_{oc} as the V_{fb} all move positively.

3.4. Electron transport

It is known that the donor concentration greatly affects the electron transport behaviors in semiconductor electrodes. However, no quantitative assessment of the TiO$_2$ donor concentration change after plasma treatment has been reported. In this study, we calculate the donor concentration before and after plasma treatment from MS measurements above and the results are also shown in Table 2. It can be seen that the N_d for blank sample is 8.51×10^{15}, while it increases to 9.30×10^{15} and 12.9×10^{15} for OP and NP, respectively. These increased donor concentrations will enhance the electron transport within the rutile array. On the contrary, the donor concentration for HP decreases to 5.54×10^{15} after plasma treatment, which will restrain the charge transfer within the electrode. Considering previous researches about the notion of trapping–detrapping process [43,44], we believe that such donor concentration difference might be due to the change of the inner chemical states of the Ti and O species caused by plasma treatments. That is, in the process of plasma treatments, some Ti^{4+} ions might transfer to Ti^{3+}. These increased Ti^{3+} 3d^1 sub-bandgap states will prohibit the electrons from being trapped and therefore improve
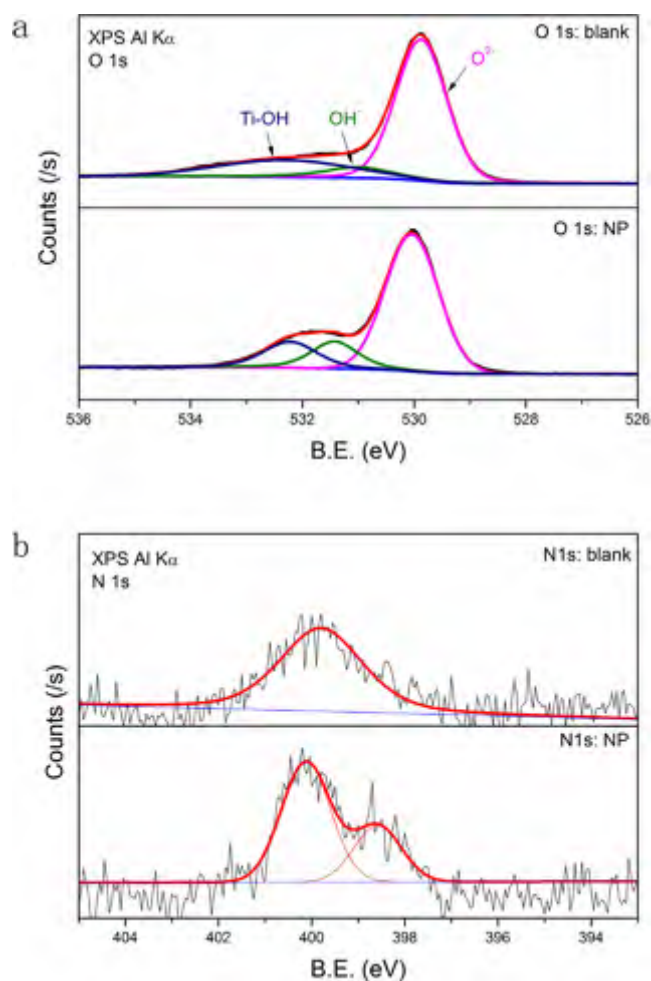

Fig. 5. XPS high resolution spectra of blank sample and NP. (a) is O 1s high resolution spectrum and (b) is N 1s.

the electron transport. Meanwhile, the rise of Ti^{3+} concentration means more oxygen vacancies are produced after surface treatment, which will also increase the donor concentration of the thin film [45].

Thus, XPS spectra measurements were carried out to clarify the changes of surface states after plasma treatment. Fig. 5 shows high resolution O 1s and N 1s XPS spectra of the untreated and nitrogen plasma treated samples (all the XPS spectra, including hydrogen and oxygen plasma treated, are shown in SI, Section 4). Fig. 5a shows the O 1s high resolution spectra of the two samples. The fitting results imply that three types of oxygen species exist at the surface of samples, which can be recognized as oxygen in O^{2-} (TiO$_2$), oxygen in OH$^-$ (Ti$_2$O$_3$) and surface hydroxyl oxygen (Ti-OH), respectively [24]. The peak area ratio of Ti$_2$O$_3$/TiO$_2$ increases from 0.126 to 0.212 after nitrogen plasma treatment, indicating that nonstoichiometric Ti$_2$O$_3$ (Ti^{3+}) species increases, which also means that more oxygen vacancies are generated and the donor concentration may increase. For HP and OP, we can also learn from Table S1 that the ratio changes to 0.117 and 0.155, respectively. Such surface state changes of rutile array coincide with the variation of calculated donor concentrations, which convinces us that the surface chemical states, especially Ti$_2$O$_3$ (Ti^{3+} and oxygen vacancies) affects the electron transport of rutile arrays.

Additionally, for NP, we have also noticed the doping effect of N after plasma treatment. As in Fig. 5b, only one peak near 400 eV can be distinguished in the N 1s high resolution spectrum of the blank sample, which is believed to be the absorbed N$_2$ on the rutile array
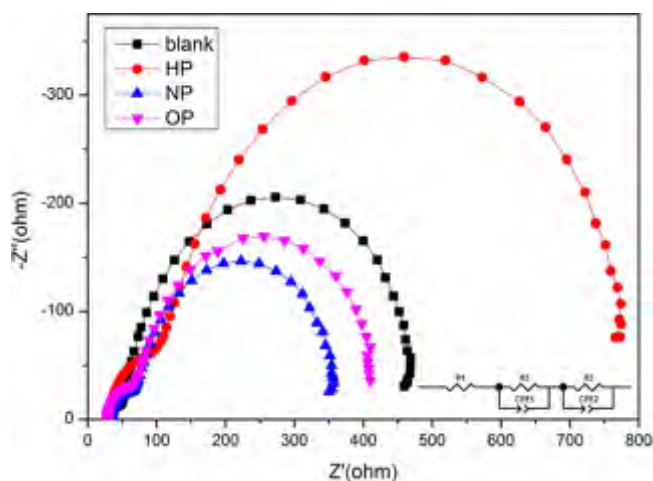
Fig. 6. Nyquist plots of plasma treated DSSCs assembled by rutile nanorod arrays.

Fig. 7. Linear sweep voltammetry curves of plasma treated DSSCs assembled by rutile nanorod arrays.

surface. Yet for NP, the N 1s spectrum can be separated into two fractions: one is the absorbed N_2 at 400 eV, the other is at 398.4 eV. Although the XPS N 1s high resolution spectrum in TiO_2 is still controversial in the community, our results are similar to that of Ma et al. [46], and we believe that the peak at 398.4 eV refers to the O—Ti—N structure, which is suggested to proceed during the substitution doping process. Since the N atomic content increases from 0.53% in the blank sample to 0.81% in NP, the slightly N-doping effect can also promote the production of $TiO_{2-x}N_x$, contributing to the donor concentration increment in NP.

The above MS plot measurements provide useful information about the electron transport behavior of the semiconductor half cells. Furthermore, electron transport performances of the whole cell under illumination are also characterized using EIS measurements. Fig. 6 presents the typical Nyquist patterns between 0.1 Hz and 100 kHz at an applied bias of V_{oc}, with the inset of Fig. 6 depicting the equivalent circuit model [47,48] In general, two typical semicircles can be interpreted into two resistances in the plot. The smaller left semicircle represents the resistance of electrolyte/Pt electrode (R_{ce}) and the larger right one shows the charge transfer resistance (R_{ct}) of the semiconductor-electrolyte interface (SEI).

From Fig. 6, we can notice that the values of R_{ce} are almost the same in the samples, indicating a similar working condition of the Pt counter electrode. However, the R_{ct} values distinguish remarkably from one another. It can be noticed that the R_{ct} for the blank sample is 455 Ω, and it decreases to 315 and 370 Ω for NP and OP, respectively. On the contrary, the R_{ct} for HP increases to 736 Ω. It is generally known that smaller R_{ct} represents better electron transport in the cell. Therefore, it can be concluded that the electron transport is improved by NP and OP, respectively, while becomes worse by HP. Interestingly, the R_{ct} decreases in the order of HP, blank sample, OP and NP, while N_d just increases in the same order. As all the dye loading amounts of plasma treated samples have increased, the consistency between R_{ct} and N_d concentration means that the N_d concentration of the photoanode might determine the charge transfer in the cells. As a result, nitrogen and oxygen plasma treatments play positive roles and enhance the charge transfer both in the rutile nanorod array photoanode and in the cell, while hydrogen plasma restricts the charge transfer.

3.5. Electron–hole recombination

Macro photoelectrochemical (PEC) tests shown in SI (Fig. S5) briefly illustrate the recombination behavior of the half cells. As Fig. S3 shows, the photocurrents for NP and OP are higher than that for the blank sample, whereas that for HP is a bit lower. It
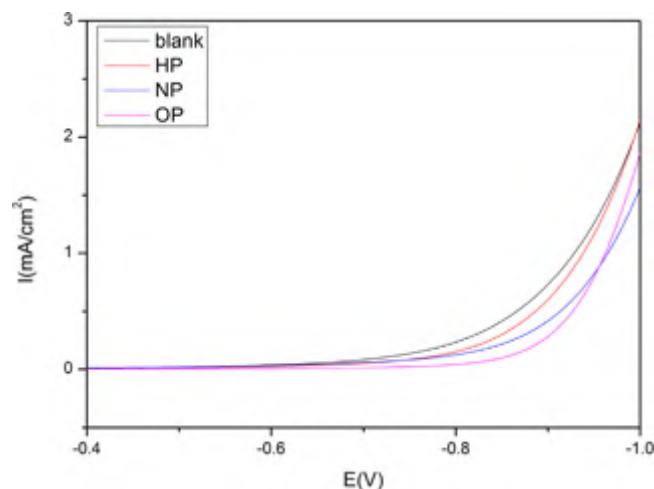
can be inferred from the PEC test that nitrogen and oxygen plasma treatment can improve the electron–hole separation and restrain the recombination in the semiconductor electrode, while hydrogen plasma treatment shows a slightly detrimental effect.

To directly investigate the recombination in the whole cells, dark current leakage test have also been taken. The dark current of a DSSC is mainly due to the back redox reaction of electrolyte, i.e., the I_3^- to I^- reduction reaction, near the photoanode [49]. The dark current represents the charge recombination and surface trap effect near the SEI [50]. The results are shown in Fig. 7. As seen from the figure, the onset potential is about 0.6 V for the blank sample, HP and NP, while it increases to about 0.8 V for OP. Moreover, under a higher bias, the dark current values become different from one other. For example, under 0.9 V bias, the dark current is 0.73, 0.60, 0.29, 0.42 mA/cm² for the blank sample, HP, OP and NP, respectively. These dark current differences represent their discrepancies in surface trap states [51], which is consistent with those of the above PEC test.

The electron life time (τ_n) is normally considered as a kinetic parameter to describe the electron recombination of the DSSC [52–54]. It is a derived parameter from OCVD test, obeying the following Eq. (2):

$$\tau_n = \frac{-k_B T}{e} \cdot \left(\frac{dV}{dt} \right)^{-1} \tag{2}$$

where k_B is the Boltzmann constant, T is the absolute temperature, e is the elementary electron charge and dV/dt is the first order differential of OCVD curve. It can be easily inferred from Eq. (2) that τ_n is shorter when the measured curve has a higher slope of measured potential over time (i.e., decayed faster). Fig. 8a shows the voltage-time decay curve and Fig. 8b shows the calculated τ_n vs. potential plot in a logarithmic presentation. It can be seen that the τ_n decreases in the order of NP, OP, HP and blank sample, especially in the low voltage region. For example, at −0.7 V, τ_n of NP is 2.35 s, and that of OP is 1.89 s, while those of HP and the blank sample are 1.62 s. The longer τ_n of NP and OP than that of the blank sample implies a lower charge recombination, and consequently, more electrons can be expected to be collected by FTO substrates. In contrast, no electron lifetime change is observed after HP treatment, implying that the hydrogen plasma shows no beneficial impact on recombination constraint.

Both the test results in the half cells and in the whole cells show that nitrogen and oxygen plasma treatments restrain the recombination yet the hydrogen plasma treatment does not. This
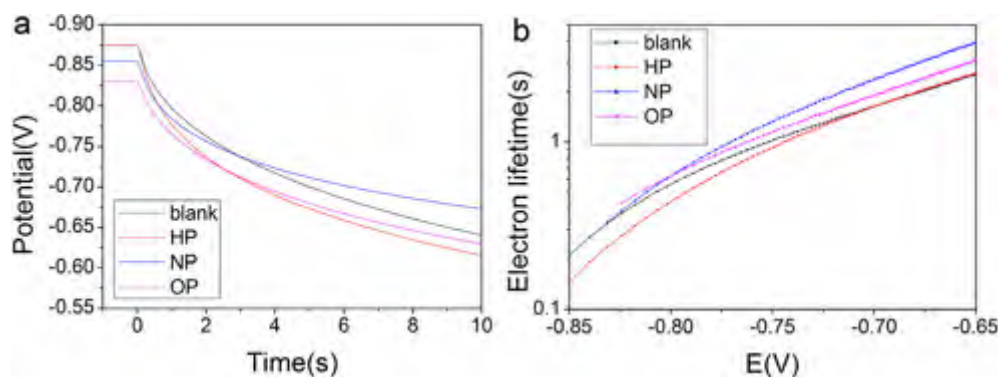
Fig. 8. Open-circuit voltage decay curves of plasma treated DSSCs assembled by rutile nanorod arrays. (a) is the voltage-time decay curve and (b) is the calculated electron lifetime (presented logarithmically) vs. voltage.
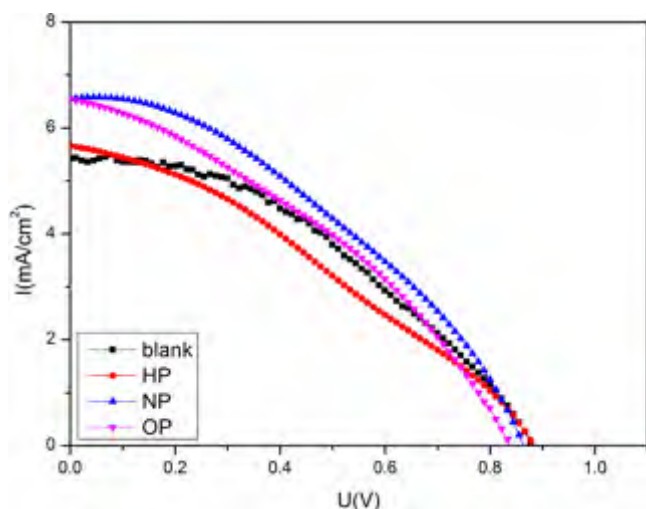

Fig. 9. Photocurrent–voltage characteristics of plasma treated DSSCs assembled by rutile nanorod arrays.

is coherent with the electron transport trend discussed in Section 3.4.

3.6. Cell performances

Fig. 9 shows photovoltaic performances of assembled DSSCs measured under AM1.5G irradiation. The photovoltaic parameters of the DSSCs are calculated from the obtained I–V curves, including the short circuit photocurrent density (J_{sc}), the open circuit voltage (V_{oc}), the cell fill factor (FF), and the power conversion efficiency (PCE). Specifically, PCE obeys Eq. (3):

$$PCE = \frac{V_{max} \cdot J_{max}}{P_{in}} \times 100\% = \frac{V_{OC} \cdot J_{SC} \cdot FF}{P_{in}} \times 100\% \qquad (3)$$

The P_{in} represents the power of light source, i.e., 100 mW/cm^2 under AM1.5G irradiation, and V_{max} and J_{max} are the voltage and the current density under the maximum output condition, respectively.

The photovoltaic parameters of DSSCs are listed in Table 3, which shows the corresponding effect of three types of plasma post-treatment. The V_{oc} of the blank sample is about 0.875 V, which is relatively higher than those reported for anatase TiO$_2$-based DSSCs. This is due to the higher conduction band of rutile than anatase. Compared with the blank sample, the V_{oc} of HP shows no change, while those of NP and OP undergo a decrease of 0.012 V and 0.045 V, respectively. These small decreases of V_{oc} in NP and OP should be attributed to the positive movement of V_{fb} discussed

Table 3
Summary of detailed parameters of plasma treated DSSCs.

Samples	Voc (V)	Jsc (mA/cm^2)	FF	EFF/%
Blank	0.875	5.4	41.6	1.90
HP	0.875	5.6	32.1	1.62
NP	0.865	6.6	38.2	2.15
OP	0.830	6.6	36.8	2.00

in Section 3.3. However, turning to the J_{sc}, the cell exhibits a relatively lower current density compared with those based on rutile nanorod arrays by previous researches [14,21]. This is mainly due to the insufficient dye loading amount resulting from the much shorter nanorods utilized in our present work, as can be seen from SEM images in Fig. 3. In this experiment, the current densities of NP and OP are both ca. 6.5 mA/cm^2, much higher than that of ca. 5.5 mA/cm^2 for the blank sample. This should be a combined result of the higher dye uptake, the increased N_d and the retarded recombination after plasma treatment. While for HP, in spite of a nearly 35% increment in the dye loading amount, the results obtained in Sections 3.4 and 3.5 indicate that the hydrogen plasma treatment leads to poorer electron transport and more severe recombination. These two counteracting effects make the J_{sc} of HP exhibit almost no change compared to that of the blank sample. As a result, NP shows a highest photo-to-electricity conversion efficiency of 2.15%, followed by 2.00% for OP, 1.90% for the blank sample and 1.62% for HP. These overall efficiency results demonstrate that nitrogen and oxygen plasma treatment are beneficial for DSSC performance, while hydrogen treatment leads to a negative effect.

4. Conclusions

Three types of plasmas (hydrogen, oxygen and nitrogen) are introduced to improve the performance of DSSCs based on rutile nanorod array photanodes. It is found that the post-treatments affect the surface roughness and hydrophilicity and further increase the dye loading of the photoanodes. After nitrogen and oxygen plasma treatments, although the flat-band potentials of NP and HP move positive for a little, which slightly reduces the V_{oc} of the cell, the N_d value increase. As a result, the electron transport is enhanced and the charge recombination is effectively restrained. For HP, the hydrogen plasma contrarily reduces the N_d of the sample, which leads to worse charge transfer and more severe recombination. Comprehensively, the NP and OP show 13% and 5% enhancement in the overall efficiency compared to the sample without treatment, whereas, the HP causes a 15% reduction in efficiency.

Acknowledgements

Appendix A. Supplementary data

Supplementary data associated with this article can be found, in the online version, at http://dx.doi.org/10.1016/j.apsusc.2014.10.099.

References

[1] B. Oregan, M. Gratzel, A low-cost, high-efficiency solar-cell based on dye-sensitized colloidal TiO2 films, Nature 353 (1991) 737–740.
[2] U. Bach, D. Lupo, P. Comte, J.E. Moser, F. Weissortel, J. Salbeck, H. Spreitzer, M. Gratzel, Solid-state dye-sensitized mesoporous TiO2 solar cells with high photon-to-electron conversion efficiencies, Nature 395 (1998) 583–585.
[3] M. Gratzel, Photoelectrochemical cells, Nature 414 (2001) 338–344.
[4] M. Gratzel, Dye-sensitized solar cells, J. Photochem. Photobiol. C: Photochem. Rev. 4 (2003) 145–153.
[5] J. Zhang, S.Q. Li, H. Ding, Q.T. Li, B.Y. Wang, X.N. Wang, H. Wang, Transfer and assembly of large area TiO2 nanotube arrays onto conductive glass for dye sensitized solar cells, J. Power Sources 247 (2014) 807–812.
[6] C.L. Chen, T.W. Chang, S.C. Su, H.S. Teng, Y.L. Lee, High performance solid-state dye-sensitized solar cells based on poly(acrylonitrile-co-vinyl acetate)/TiO2 nanoparticles redox electrolytes, J. Power Sources 247 (2014) 406–411.
[7] J.Z. Chen, J.Q. Luo, X.H. Jin, Y.Q. Liu, J. Sun, L. Gao, Promotion of charge transport in low-temperature fabricated TiO2 electrodes by curing-induced compression stress, Electrochim. Acta 100 (2013) 85–92.
[8] F. Shao, J. Sun, L. Gao, J.Z. Chen, S.W. Yang, Electrophoretic deposition of TiO2 nanorods for low-temperature dye-sensitized solar cells, RSC Adv. 4 (2014) 7805–7810.
[9] J.T. Jiu, S. Isoda, F.M. Wang, M. Adachi, Dye-sensitized solar cells based on a single-crystalline TiO2 nanorod film, J. Phys. Chem. B 110 (2006) 2087–2092.
[10] S.H. Kang, S.H. Choi, M.S. Kang, J.Y. Kim, H.S. Kim, T. Hyeon, Y.E. Sung, Nanorod-based dye-sensitized solar cells with improved charge collection efficiency, Adv. Mater. 20 (2008) 54.
[11] F. Shao, J. Sun, L. Gao, S.W. Yang, J.Q. Luo, Forest-like TiO2 hierarchical structures for efficient dye-sensitized solar cells, J. Mater. Chem. 22 (2012) 6824–6830.
[12] G.K. Mor, K. Shankar, M. Paulose, O.K. Varghese, C.A. Grimes, Use of highly-ordered TiO2 nanotube arrays in dye-sensitized solar cells, Nano Lett. 6 (2006) 215–218.
[13] K. Zhu, N.R. Neale, A. Miedaner, A.J. Frank, Enhanced charge-collection efficiencies and light scattering in dye-sensitized solar cells using oriented TiO2 nanotubes arrays, Nano Lett. 7 (2007) 69–74.
[14] B. Liu, E.S. Aydil, Growth of oriented single-crystalline rutile TiO2 nanorods on transparent conducting substrates for dye-sensitized solar cells, J. Am. Chem. Soc. 131 (2009) 3985–3990.
[15] K.K. Tehare, M.K. Zate, S.S. Bhande, S.A. Patil, S.L. Gaikwad, S.J. Yoon, R.S. Mane, S.H. Lee, S.H. Han, Effect of a deposition container on the nanostructural growth and DSSC application of rutile TiO2, J. Mater. Chem. A 2 (2014) 478–483.
[16] H. Yu, J. Pan, Y. Bai, X. Zong, X.Y. Li, L.Z. Wang, Hydrothermal synthesis of a crystalline rutile TiO2 nanorod based network for efficient dye-sensitized solar cells, Chem. Eur. J. 19 (2013) 13569–13574.
[17] X. Tan, P. Qiang, D. Zhang, X. Cai, S. Tan, P. Liu, W. Mai, Three-level hierarchical TiO2 nanostructure based high efficiency dye-sensitized solar cells, CrystEngComm 16 (2014) 1020–1025.
[18] M.J. Yang, S. Neupane, X.W. Wang, J. He, W.Z. Li, N. Pala, Multiple step growth of single crystalline rutile nanorods with the assistance of self-assembled monolayer for dye sensitized solar cells, ACS Appl. Mater. Interfaces 5 (2013) 9809–9815.
[19] J.Y. Wang, T.J. Zhang, D.F. Wang, R.K. Pan, Q.Q. Wang, H.M. Xia, Improved morphology and photovoltaic performance in TiO2 nanorod arrays based dye sensitized solar cells by using a seed layer, J. Alloy. Compd. 551 (2013) 82–87.
[20] S.S. Mali, H. Kim, C.S. Shim, W.R. Bae, N.L. Tarwal, S.B. Sadale, P.S. Patil, J.H. Kim, C.K. Hong, Single-step synthesis of 3D nanostructured TiO2 as a scattering layer for vertically aligned 1D nanorod photoanodes and their dye-sensitized solar cells, CrystEngComm 15 (2013) 5660–5667.
[21] M. Lv, D. Zheng, M. Ye, L. Sun, J. Xiao, W. Guo, C. Lin, Densely aligned rutile TiO2 nanorod arrays with high surface area for efficient dye-sensitized solar cells, Nanoscale 4 (2012) 5872.
[22] S.M. Wang, W.W. Dong, R.H. Tao, Z.H. Deng, J.Z. Shao, L.H. Hu, J. Zhu, X.D. Fang, Optimization of single-crystal rutile TiO2 nanorod arrays based dye-sensitized solar cells and their electron transport properties, J. Power Sources 235 (2013) 193–201.
[23] Y. Ling, J.K. Cooper, Y. Yang, G. Wang, L. Munoz, H. Wang, J.Z. Zhang, Y. Li, Chemically modified titanium oxide nanostructures for dye-sensitized solar cells, Nano Energy 2 (2013) 1373–1382.
[24] H.J. Kim, J. Kim, B. Hong, Effect of hydrogen plasma treatment on nanostructured TiO2 films for the enhanced performance of dye-sensitized solar cell, Appl. Surf. Sci. 274 (2013) 171–175.
[25] J. Wang, Z. Lin, Dye-sensitized TiO2 nanotube solar cells with markedly enhanced performance via rational surface engineering, Chem. Mater. 22 (2010) 579–584.
[26] H.S. Kim, J.W. Lee, N. Yantara, P.P. Boix, S.A. Kulkarni, S. Mhaisalkar, M. Grätzel, N.G. Park, High efficiency solid-state sensitized solar cell-based on submicrometer rutile TiO2 nanorod and CH3NH3PbI3 perovskite sensitizer, Nano Lett. 13 (2013) 2412–2417.
[27] H. Cheng, J. Ma, Z. Zhao, L. Qi, Hydrothermal preparation of uniform nanosize rutile and anatase particles, Chem. Mater. 7 (1995) 663–671.
[28] J. Zhang, M.J. Li, Z.C. Feng, J. Chen, C. Li, UV Raman spectroscopic study on TiO2. I. Phase transformation at the surface and in the bulk, J. Phys. Chem. B 110 (2006) 927–935.
[29] K. Ahn, Y.S. Jeong, H.U. Lee, S.Y. Jeong, H.S. Ahn, H.S. Kim, S.G. Yoon, C.R. Cho, Physical properties of hydrogenated Al-doped ZnO thin layer treated by atmospheric plasma with oxygen gas, Thin Solid Films 518 (2010) 4066–4070.
[30] K. Ahn, H.-U. Lee, S.-Y. Jeong, J.-P. Kim, J.S. Jin, H.-S. Ahn, H.-S. Kim, C.-R. Cho, Plasma treatment effect on dye-sensitized solar cell efficiency of hydrothermal-processed TiO2 nanorods, J. Nanosci. Nanotechnol. 12 (2012) 6022–6025.
[31] E. Levrau, K. Devloo-Casier, J. Dendooven, K.F. Ludwig, P. Verdonck, J. Meersschaut, M.R. Baklanov, C. Detavernier, Atomic layer deposition of TiO2 on surface modified nanoporous low-k films, Langmuir 29 (2013) 12284–12289.
[32] H.C. Barshilia, N. Gupta, Superhydrophobic polytetrafluoroethylene surfaces with leaf-like micro-protrusions through Ar + O2 plasma etching process, Vacuum 99 (2014) 42–48.
[33] K. Guo, M. Li, X. Fang, M. Luoshan, L. Bai, X. Zhao, Performance enhancement in dye-sensitized solar cells by utilization of a bifunctional layer consisting of core–shell β-NaYF4:Er3+/Yb3+@SiO2 submicron hexagonal prisms, J. Power Sources 249 (2014) 72–78.
[34] W.G. Wang, H.Y. Zhang, R. Wang, M. Feng, Y.M. Chen, Design of a TiO2 nanosheet/nanoparticle gradient film photoanode and its improved performance for dye-sensitized solar cells, Nanoscale 6 (2014) 2390–2396.
[35] W.S. Man, C.W. Kan, S.P. Ng, The use of atmospheric pressure plasma treatment on enhancing the pigment application to cotton fabric, Vacuum 99 (2014) 7–11.
[36] G.A. Samara, P.S. Peercy, Pressure and temperature-dependence of static dielectric-constants and raman-spectra of TiO2 (rutile), Phys. Rev. B 7 (1973) 1131–1148.
[37] I. Mora-Seró, F. Fabregat-Santiago, B. Denier, J. Bisquert, R. Tena-Zaera, J. Elias, C. Lévy-Clément, Determination of carrier density of ZnO nanowires by electrochemical techniques, Appl. Phys. Lett. 89 (2006).
[38] O. Ozcan, K. Pohl, P. Keil, G. Grundmeier, Effect of hydrogen and oxygen plasma treatments on the electrical and electrochemical properties of zinc oxide nanorod films on zinc substrates, Electrochem. Commun. 13 (2011) 837–839.
[39] Z. Endut, M. Hamdi, W.J. Basirun, An investigation on formation and electrochemical capacitance of anodized titania nanotubes, Appl. Surf. Sci. 280 (2013) 962–966.
[40] H. Liu, G. Piret, B. Sieber, J. Laureyns, P. Roussel, W. Xu, R. Boukherroub, S. Szunerits, Electrochemical impedance spectroscopy of ZnO nanostructures, Electrochem. Commun. 11 (2009) 945–949.
[41] J. Bandara, U.W. Pradeep, Tuning of the flat-band potentials of nanocrystalline TiO2 and SnO2 particles with an outer-shell MgO layer, Thin Solid Films 517 (2008) 952–956.
[42] M.-H. Kim, Y.-U. Kwon, Semiconductor CdO as a blocking layer material on DSSC electrode: mechanism and application, J. Phys. Chem. C 113 (2009) 17176–17182.
[43] X. Lü, X. Mou, J. Wu, D. Zhang, L. Zhang, F. Huang, F. Xu, S. Huang, Improved-performance dye-sensitized solar cells using Nb-doped TiO2 electrodes: efficient electron injection and transfer, Adv. Funct. Mater. 20 (2010) 509–515.
[44] H.J. Snaith, L. Schmidt-Mende, Advances in liquid-electrolyte and solid-state dye-sensitized solar cells, Adv. Mater. 19 (2007) 3187–3200.
[45] A. Janotti, J.B. Varley, P. Rinke, N. Umezawa, G. Kresse, C.G. Van de Walle, Hybrid functional studies of the oxygen vacancy in TiO2, Phys. Rev. B 81 (2010) 085212.
[46] T.L. Ma, M. Akiyama, E. Abe, I. Imai, High-efficiency dye-sensitized solar cell based on a nitrogen-doped nanostructured titania electrode, Nano Lett. 5 (2005) 2543–2547.
[47] J. Bisquert, Theory of the impedance of electron diffusion and recombination in a thin layer, J. Phys. Chem. B 106 (2002) 325–333.
[48] Q. Wang, J.E. Moser, M. Gratzel, Electrochemical impedance spectroscopic analysis of dye-sensitized solar cells, J. Phys. Chem. B 109 (2005) 14945–14953.
[49] B. Li, J. Chen, J. Zheng, J. Zhao, Z. Zhu, H. Jing, Photovoltaic performance enhancement of dye-sensitized solar cells by formation of blocking layers via molecular electrostatic effect, Electrochim. Acta 59 (2012) 207–212.
[50] K. Tennakone, P.V.V. Jayaweera, P.K.M. Bandaranayake, Dye-sensitized photoelectrochemical and solid-state solar cells: charge separation, transport and

recombination mechanisms, J. Photochem. Photobiol. A: Chem. 158 (2003) 125–130.

[51] H. Yu, S. Zhang, H. Zhao, B. Xue, P. Liu, G. Will, High-performance TiO$_2$ photoanode with an efficient electron transport network for dye-sensitized solar cells, J. Phys. Chem. C 113 (2009) 16277–16282.

[52] K. Sunahara, J. Ogawa, S. Mori, A method to measure electron lifetime in dye-sensitized solar cells: stepped current induced measurement of cell voltage in the dark, Electrochem. Commun. 13 (2011) 1420–1422.

[53] A. Zaban, M. Greenshtein, J. Bisquert, Determination of the electron lifetime in nanocrystalline dye solar cells by open-circuit voltage decay measurements, ChemPhysChem 4 (2003) 859–864.

[54] S. Nakade, T. Kanzaki, Y. Wada, S. Yanagida, Stepped light-induced transient measurements of photocurrent and voltage in dye-sensitized solar cells: application for highly viscous electrolyte systems, Langmuir 21 (2005) 10803–10807.